




Preparation of $W_{0.4}Mo_{0.6}O_3$ from Secondary Resources by a Simple Heat-Treatment Process and Discussion of Its Superior Selective Adsorption Properties

YANAN LIU,¹ YANGSI LIU,^{1,3} LIWEN MA,^{1,2,3} XIAOLI XI ^{1,2,4}
and ZUOREN NIE^{1,2,3}

1.—Collaborative Innovation Center of Capital Resource-Recycling Material Technology, Beijing University of Technology, Beijing 100124, China. 2.—Key Laboratory of Advanced Functional Materials, Ministry of Education, Faculty of Materials and Manufacturing, Beijing University of Technology, Beijing 100124, China. 3.—National Engineering Laboratory for Industrial Big-Data Application Technology, Beijing University of Technology, Beijing 100124, China. 4.—e-mail: xixiaoli@bjut.edu.cn

Tungsten molybdenum oxide ($W_{0.4}Mo_{0.6}O_3$) was prepared by a simple heat-treatment process using ion exchange resins as the template. The morphology and crystallinity of the product can be controlled by varying the calcination temperature. The products show excellent selective adsorption properties for methylene blue (MB) and rhodamine B model dyes with different molecular sizes and charges, especially for MB. The kinetic data show that the product accords with the pseudo-second-order kinetic model, and the adsorption isotherm can be described by the Langmuir adsorption isotherm. When the concentration of MB was 100 mg/L, the adsorption capacity of the product calcined at 300°C and the primary W/Mo molar ratio of 1:1 can be 833.43 mg/g, which is higher than that reported in the literature. Electrostatic adsorption was found to be the main adsorption mechanism. This article presents a heat treatment method to obtain tungsten molybdenum oxide from W-Mo alloy scrap, showing an easy method for the utilization of secondary sources for environmental remediation.

INTRODUCTION

Tungsten (W) and molybdenum (Mo) are both refractory rare metal elements. W is used widely in metallurgy,^{1–3} the chemical industry,^{4–6} medicine,⁷ electronics,⁸ etc. Mo and its alloys also have a wide range of applications and good prospects in important sectors such as metallurgy,⁹ agriculture,¹⁰ electrical,¹¹ chemical industry,^{12,13} and aerospace,¹⁴ etc. Due to the wide application of W and Mo as structural materials, the demand for W and Mo resources is increasing worldwide, and the amount of W and Mo waste also continues to rise. In 2020, the global recovery of Mo resources was 110,000 tons, accounting for ~ 27% of the total Mo supply, while the global average recovery rate of W

accounted for only 35% of the supply.^{15,16} Compared with the total supply, the recovery of W and Mo is much lower.

The recovery and reuse of W and Mo from waste resources have become a research hotspot in recent years. W and Mo belong to the same subgroup, and due to the effect of “lanthanide shrinkage”, the atomic radius and chemical properties of the two elements are very similar, and they often exist together in the form of tungstate and molybdate in minerals and are difficult to separate.¹⁶ Most of the wastes containing both W and Mo are separated by wet chemical methods, such as the extraction method,¹⁷ ion exchange method,¹⁸ precipitation method,¹⁹ and so on. Most separation methods change the existing state of W and Mo ions in the solution by adjusting the pH value. They can also be separated by introducing some element or substance to expand the gap between them. However,

(Received October 21, 2022; accepted May 22, 2023;
published online June 16, 2023)

no matter which method is adopted, the separation and extraction process of W and Mo into isolated metals is relatively long and consumes humanpower and material resources.

The preparation of functional materials without the separation procedure can be another way to recover these two valuable metals, which undoubtedly greatly shortens the time and realizes the circular development of resources. In recent years, many studies have prepared functional materials through a relatively short process of extracting and utilizing metal elements simultaneously. Yakun Zhang et al.²⁰ proposed an effective method to prepare two useful alloys, Ti_5Si_3 and $Ti_5Si_4-TiAl_3$, from three kinds of waste. Using aluminum alloy waste as a reducing agent, Ti and Si were extracted from waste SCR catalyst and titanium-bearing blast furnace slag, and Ti-Si-Al alloy was prepared at the same time. Liang et al.²¹ did not extract Li and Co from waste electrode materials respectively but repaired $LiCoO_2$ materials directly, and the properties of the repaired $LiCoO_2$ were greatly improved. Deng et al.²² did not separate the metal elements in scrapped lithium batteries, but directly recovered the degraded ternary cathode materials in the presence of acetylene black, so that the degraded $LiNi_{0.5}Co_{0.2}Mn_{0.3}O_2$ particles could directly restore the original $\alpha-NaFeO_2$ structure and be reused. However, the above studies are all about anode materials in waste batteries; the research on directly using W and Mo in waste without separation and to make them into functional materials has not been reported.

In this article, W and Mo were extracted indiscriminately with D201 resin from the simulated waste, and tungsten molybdenum oxide was prepared by a heat-treatment process. A series of characterizations were carried out on the prepared samples, and it was found that the product had superior adsorption to methylene blue (MB), which shows great environmental function, and provides a new clue for resource recycling.

EXPERIMENTAL

Synthesis

Sodium tungstate, sodium molybdate, ion exchange resin (D201), methylene blue, and hydrochloric acid (37%) were of analytical grade and used without further purification.

The solution containing tungsten and molybdenum ions is used to simulate the treated solution of tungsten and molybdenum waste. Sodium tungstate and sodium molybdate with a W/Mo molar ratio of 1:1 were dissolved in 50 mL deionized water, and hydrochloric acid was added to adjust pH to 3.5. The prepared solution was placed for 2 h to ensure that the polymerized state of the tungstate and molybdate no longer changed. After that, the pretreated ion exchange resin was added and stirred, and adsorbed for 4 h. The adsorbed resin was calcined in

an autoclave at 232°C for 1 h, and then washed with deionized water several times and dried. The dried resin was calcined in air at 300°C, 350°C, 400°C, 500°C, and 600°C, respectively, and then tungsten molybdenum oxide was obtained. The tungsten molybdenum oxide products are named after the calcination temperature, such as TMO300, TMO350, TMO400, TMO500, and TMO600.

Characterization

The X-ray diffraction patterns of all samples were measured by using an X-ray diffractometer with monochromatic $Cu K\alpha$ ($\lambda = 1.5406 \mu m$, working voltage 40 kV, current density 30 mA). The morphology and microstructure of the samples were studied by Hitachi SU9000 field emission scanning electron microscope (FESEM) under the working voltage of 10 kV. The high-resolution morphologies of the samples were studied by transmission electron microscopy (JEM-2100F, JEOL, Japan) under 200 kV acceleration voltage. The zeta potential of the sample was recorded by Zeta Potential Analyzer (Nano-ZS, Malvern, UK). X-ray photoelectron spectroscopy was identified by Escalab 250Xi electron spectrometer (Thermo Fisher Science, USA) and Al K α X-ray source. Fourier transform infrared spectrometer (FTIR-650, Guangdong FTIR-650) was used to analyze the samples in mid-infrared mode. The ultraviolet-visible light (UV-Vis) absorption spectrum was recorded by an ultraviolet-visible spectrometer (TU-1901, Purkinje, China).

Adsorption Experiments

To evaluate the adsorption capacity of samples, MB solution was used as the wastewater model; 10 mg of tungsten molybdenum oxide was added to 100 mL of MB solution (10 mg/L) and stirred in the dark. At regular intervals, 5 mL suspension was taken out and separated by centrifuge. The supernatant was taken and the absorbance was measured by UV-Vis spectrophotometer. The MB adsorption capacity in different periods was calculated according to Eq. 1, and the MB removal rate in different periods was calculated according to Eq. 2^{23,24}

$$q_t = \frac{(C_0 - C_t) \times V}{m} \quad (1)$$

$$R = \frac{(C_0 - C_t) \times 100\%}{C_0} \quad (2)$$

In formula (1) and (2), q_t (mg/g) is the adsorption amount of MB in different periods, C_0 (mg/L) is the initial concentration of MB, C_t (mg/L) is the concentration of MB at the time t (min), V (L) is the solution volume, and m (g) is the mass of tungsten molybdenum oxide. R is the removal rate of MB at different times.

To evaluate the equilibrium adsorption capacity of the sample, 10 mg of tungsten molybdenum oxide obtained was added to the 100 mL MB solution (10–300 mg/L) and stirred in the dark until the sample reached the adsorption equilibrium. Samples were taken at regular intervals for dynamic analysis. The equilibrium adsorption capacity of different MB concentrations was calculated according to Eq. 3.²⁵

$$q_e = \frac{(C_0 - C_e) \times V}{m} \quad (3)$$

In this formula, q_e (mg/L) is the equilibrium adsorption capacity of MB, and C_e (mg/L) is the equilibrium concentration of MB.

The selective adsorption properties of the products were tested with methyl orange (MO), rhodamine B (RhB), and MB. The dye selectivity experiment was carried out by adding 10 mg of samples to the mixed dye solution of 100 mL. The selective adsorption experiments of single dye solution and mixed dye solution were carried out at pH = 7.0 and room temperature.

To investigate the reusability of adsorbents on MB, adsorption-analytical cycle experiments were carried out. The adsorbent (30 mg) was added to MB solution (50 mL, 50 mg/L) and stirred at 25°C for 2 h. Then, the adsorbent was collected by centrifugation and dried in an oven at 60°C. After that, the adsorbent was calcined in the air at 300°C for 30 min to eliminate adsorbates. The calcined adsorbent could then be used in the next cycle of the experiment.

RESULTS AND DISCUSSION

Morphology and Microstructure

Figure 1a, b, c, d, and e shows the SEM diagrams of products prepared at different calcination temperatures. Figure 1a, b, and c shows that when the calcination temperature is < 400°C, the size of the sample is uneven. The morphology is an irregular flake with a certain degree of clusters. Samples are prepared with the resin as the template,²⁶ which is calcined after adsorbing tungsten and molybdenum ions, so the original porous sphere of the resin will be decomposed into flakes during the calcination. When the calcination temperature is raised to 500°C and 600°C, the size of the samples increases gradually, and the morphology of TMO500 and TMO600 is different from others. The calcination temperature not only plays an important role in the shape and the size of samples, but, as Fig. 1a, b, c, d, and e shows, the sample size increases gradually with the increase of calcination temperature.

Figure 1f shows the XRD spectra of products prepared at different calcination temperatures. The crystallinity of TMO300 and TMO350 is poor, so it is difficult to attribute it to a certain phase. However, there are strong peaks in TMO400, TMO500, and TMO600 at 23.1°, 24.7°, 26.3°, 33.5°, and 34.1°,

which are consistent with the orthorhombic phase $W_{0.4}Mo_{0.6}O_3$ (JCPDS no. 76-1280)^{27,28} and their strong peaks corresponding to crystal planes (110), (002), (111), (200), (112), respectively. Figure 1e shows that the increase in calcination temperature is beneficial to the crystallization of products.

TMO300, TMO350, and TMO400 were characterized by TEM and HRTEM as shown in Fig. 2. Figure 2a, b, and c shows that TMO300, TMO350, and TMO400 are flaky and uneven with some agglomeration, which is consistent with the results of SEM. Analyzing the HRTEM images of Fig. 3d, e, and f shows that the crystal plane spacing of TMO400 is about 0.383 nm. This is consistent with the crystal plane spacing corresponding to the (110) plane of the orthorhombic phase of $W_{0.4}Mo_{0.6}O_3$. However, the crystal structure cannot be distinguished from HRTEM images of TMO300 and TMO350, indicating the amorphous phase. This is also consistent with the results of XRD.

Comparison of Adsorption Properties

The adsorption properties of samples prepared at different calcination temperatures can be evaluated by adsorption capacity and adsorption equilibrium time, as shown in supplementary Fig. S1 (refer to online supplementary material). TMO300 has the best adsorption rate of MB at 96.83%, while the adsorption rate of TMO600 for MB is only 15.7%. The adsorption efficiency of TMO350 for MB is almost the same as that of TMO300, which is 95.41%. The adsorption rate of MB by TMO400 and TMO500 is 85.01% and 50%, respectively. The adsorption capacity of MB by TMO300 is 94.82 mg/g for 30 min, and the adsorption capacity can be 96.83 mg/g for 300 min, while it is only 15.7 mg/g for TMO600 after 300 min.

The adsorption process can be divided into the fast (first) adsorption stage and the slow (second) adsorption stage,²⁹ and the adsorption rate is mainly controlled by the external diffusion (film diffusion) rate and internal diffusion rate of the adsorbate molecules. In the process of fast adsorption, MB can be adsorbed quickly as there are a large number of adsorption sites and pores on the initial adsorbent. As time goes on, since the adsorbed MB has filled the adsorption sites and agglomerated on the sample surface, the steric hindrance increases; therefore, external MB molecules will no longer diffuse to the adsorbent, which makes the adsorption process slow.

It is found that the adsorption capacity is not only related to the properties of adsorbents and adsorbates but also the degree of shortcuts on the solid surface,^{28–30} that is to say, the state of substances on the solid surface will change the adsorption capacity. With the increase of calcination temperature, the products change from an amorphous state to a crystalline state, so that the existing state of the products' surface substances will be different, and

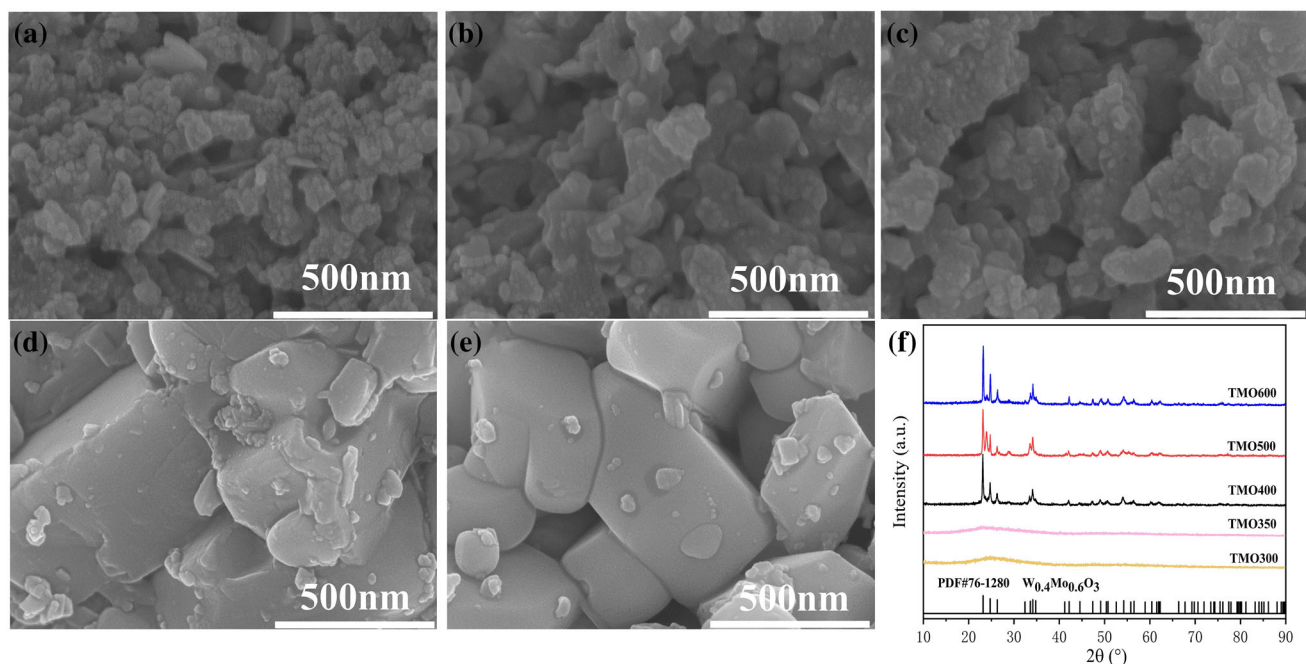


Fig. 1. SEM images of materials calcined at different temperatures: TMO300 (a), TMO350 (b), TMO400 (c), TMO500 (d), TMO600 (e). (f) XRD pattern of samples.

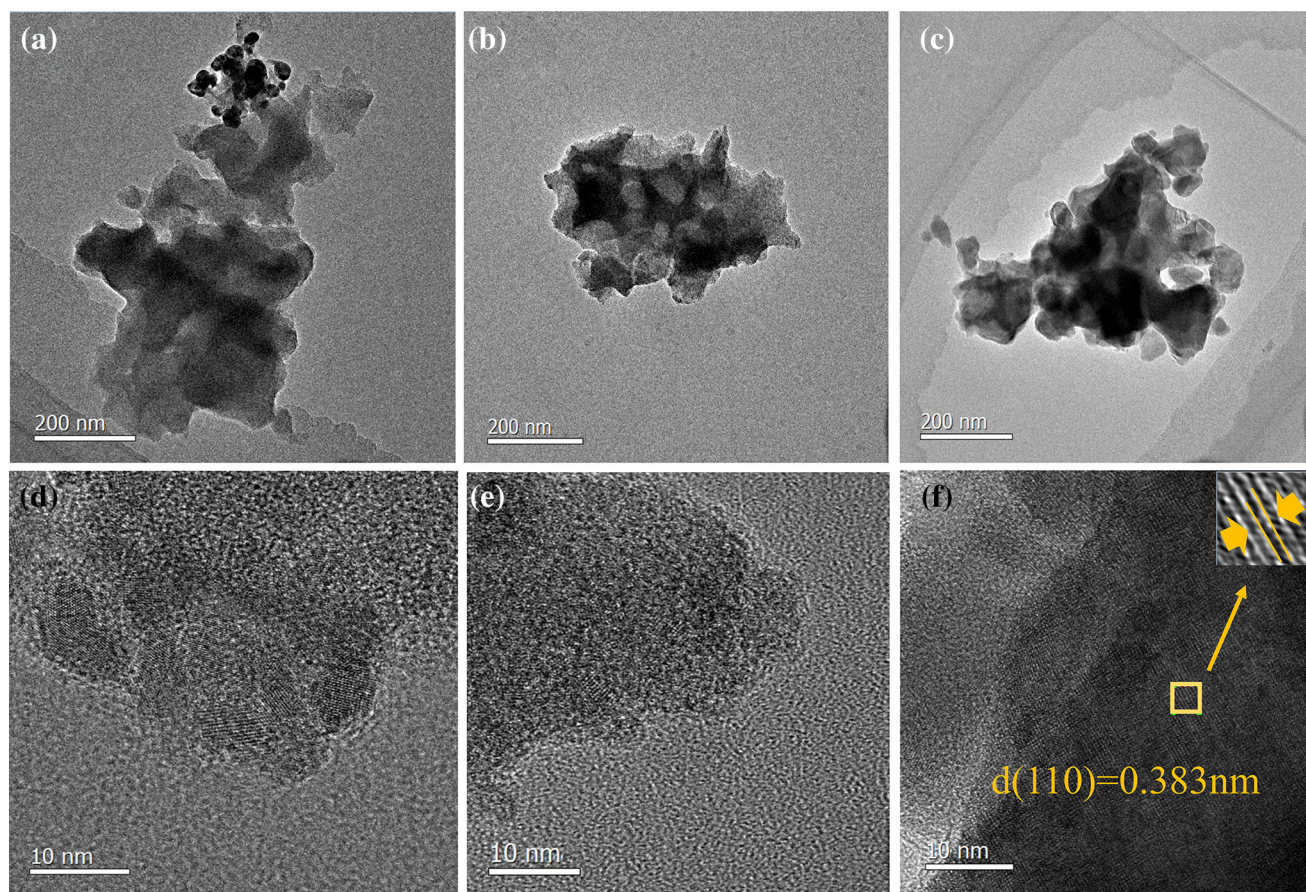


Fig. 2. TEM images of TMO300 (a), TMO350 (b), TMO400 (c), and HRTEM images of TMO300 (d), TMO350 (e), TMO400 (f).

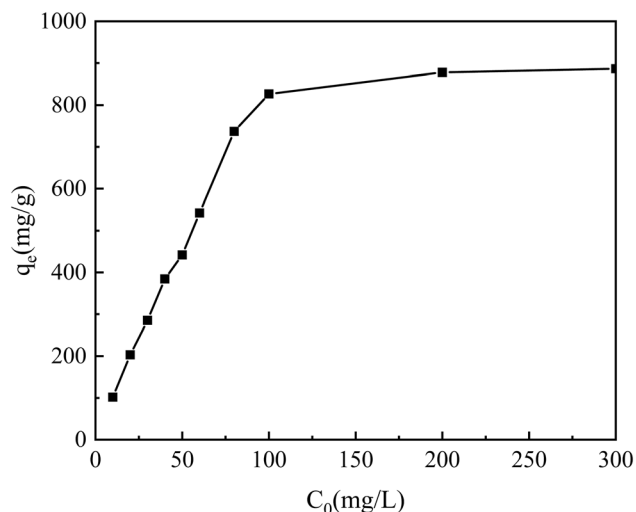


Fig. 3. Equilibrium adsorption capacity of TMO300 at different concentrations of MB.

then the adsorption capacity of the product to MB will be different. With the increase in temperature, the adsorption capacity of the products for MB gradually decreases.

Effects of Initial Concentration

To further probe the adsorption process, the influence of initial MB concentration (10-300 mg/L) on the adsorption performance of TMO300 was investigated. As shown in Fig. 3, the equilibrium adsorption capacity of TMO300 increases linearly when the initial concentration of MB is < 100 mg/L. When the initial concentration of MB is > 100 mg/L, the adsorption capacity of TMO300 does not change much and gradually tends to be stable. The initial concentration of dye is an important driving force to overcome the mass transfer resistance of dye molecules between the solid and aqueous phase.^{31,32} When the concentration of MB is low, the number of active sites in TMO300 is larger than that of MB molecules, and the number of active sites plays a decisive role in the adsorption capacity. At higher dye concentrations, the concentration gradient increases with increasing dye concentration. In other words, the higher the dye concentration is, the greater the mass transfer driving force, resulting in a higher adsorption capacity of the adsorbent. When the dye concentration increases to a certain value, the number of MB molecules is larger than the number of active sites of TMO300, which makes the adsorption of TMO300 saturated, resulting in a stable adsorption curve. Therefore, the adsorbed dye mainly depends on the initial concentration.

Adsorption Kinetics

The adsorption kinetics of solutes in solution by solid adsorbents can be described by the pseudo-first-order kinetic model, pseudo-second-order kinetic model, Weber's intraparticle diffusion

model, or Elovich adsorption kinetic model.²⁴ The adsorption kinetics can reflect the physicochemical characteristics of the adsorbent, such as the adsorption rate and diffusion process. For the details of the model, see supplementary data file S1. Figure 4 shows the adsorption kinetics with the initial concentration of 100 mg/L, and for the relevant parameters fitted by the kinetic model, see supplementary Table S1.

Comparing the fitting results of the pseudo-first-order kinetic model, pseudo-second-order kinetic model, and Elovich model, the R^2 of the pseudo-second-order kinetic model is 0.98548, which is higher than that of others indicating that the adsorption process of TMO300 is more in line with the pseudo-second-order kinetic model. This shows that the adsorption process of TMO300 is a combination of multiple adsorption mechanisms.³³ From Weber's intraparticle diffusion model fitting results of Fig. 4d, the adsorption process can be divided into two stages: film diffusion and pore diffusion. In the process of film diffusion (the first stage), MB molecules will spread to the outer surface of TMO300. Then, they will enter the pores and bind to the active sites in the process of pore diffusion (the second stage). The observed multilinearity and the fitted line do not go through the origin, indicating that the intramolecular diffusion of MB is not controlled by a single rate, and boundary layer diffusion also controls the adsorption to some extent. The slope (K_{id}) of the film diffusion stage process is greater than that of the pore diffusion stage, implying that the diffusion process is gradual. It is also found that the intraparticle diffusion of MB plays a larger role in the rate-limiting step since the pore diffusion intercept (C_1) is larger than the film diffusion intercept (C_2).³³

Adsorption Isotherms

The adsorption equilibrium data are the basis to design the adsorption system to remove organic pollutants. Many isothermal models, including Langmuir, Freundlich, and Temkin,³⁴ can not only describe the equilibrium relationship between adsorbates and adsorbents but also provide valuable information for studying the surface properties and adsorption mechanism of adsorbents. For the details of the model, see supplementary data file S2. For the isotherm model fitting diagram, see supplementary Fig. S3, and for the relevant parameters of isothermal model fitting, see supplementary Table S2 and Fig. S3.

In the fitting process of three different isothermal models, the R^2 of the Langmuir model is the largest (0.9807), indicating that the model can accord with the adsorption process of MB by TMO300 and the adsorption process is surface-controlled monolayer adsorption. The simulated maximum adsorption capacity calculated by the Langmuir model is 823.33 mg/g, slightly smaller than the maximum

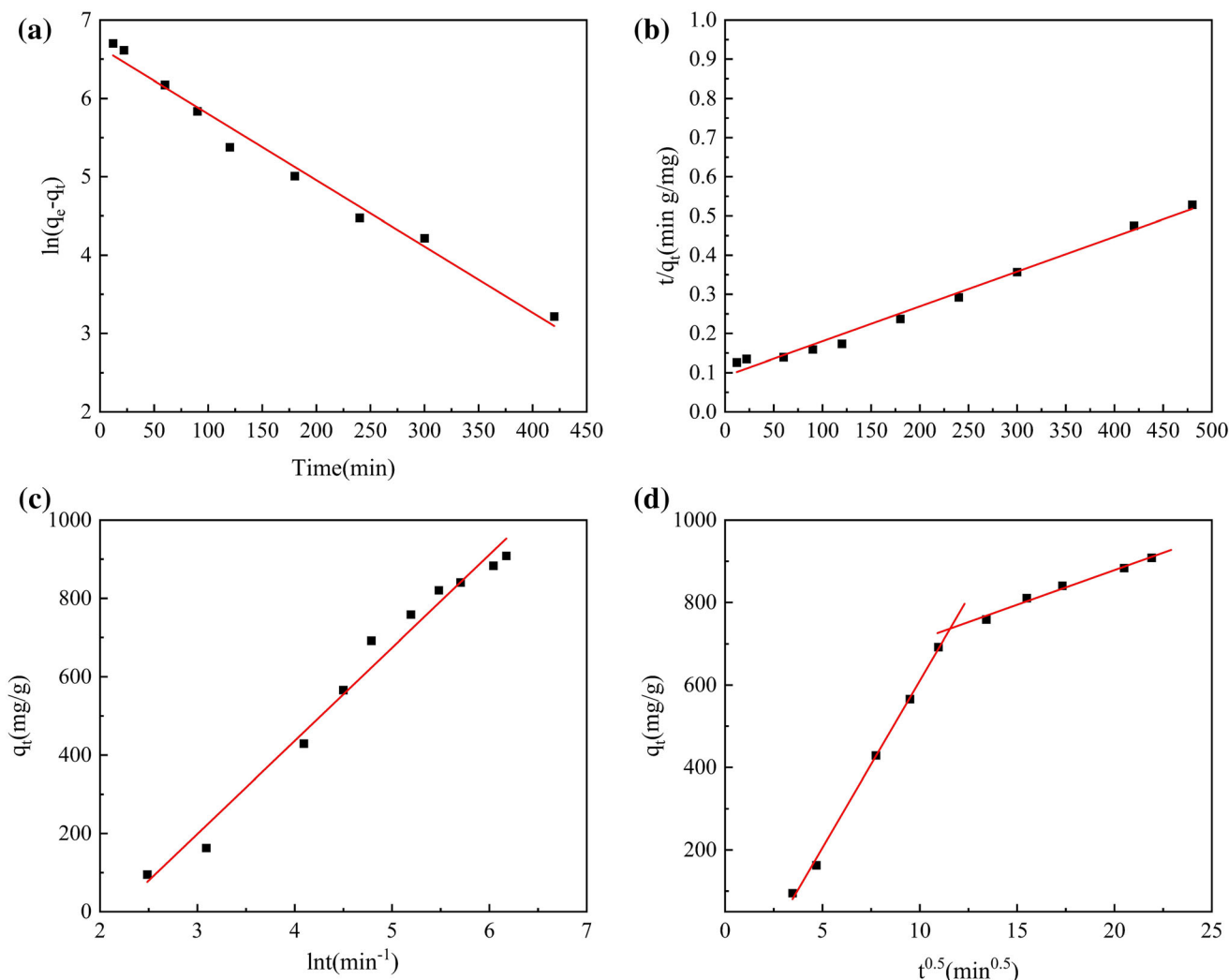


Fig. 4. The adsorption of MB by TMO300 is based on the pseudo-first-order kinetic model (a), pseudo-second-order kinetic model (b), Elovich model (c), and Weber's intraparticle diffusion model (d) fitting diagram.

Table I. Comparison of adsorption properties of different adsorbents for MB

Absorbent	pH	T (K)	C_0 (mg L ⁻¹)	m/V (mg mL ⁻¹)	q_m (mg g ⁻¹)	Refs.
Flower-like WO ₃ ·H ₂ O	7	288	100	20/20	117.8	35
Urchin-like WO ₃ ·0.33H ₂ O	7	288	100	20/20	247.3	35
2D MoS ₂ nanosheets	7	298	20	10/200	272.0	36
Layered porous MoS ₂	7	298	200	100/100	499.0	37
MoO ₃ nanorods and nanoplates	11	298	250	100/25	152.2	14
W _{0.4} Mo _{0.6} O ₃	7	298	100	10/100	833.43	This work

adsorption capacity (833.43 mg/g) obtained by our experiment, which demonstrates that there are not only uniform adsorption sites but also non-uniform adsorption sites in the samples. Table I lists the reported maximum adsorption capacities of some adsorbents containing tungsten or molybdenum. The adsorption property of tungsten molybdenum

oxides prepared in this study is better than in many literature reports.

Adsorption Mechanism

TMO300-TMO500 are electronegative in an aqueous solution (see supplementary Table S3), which enables them to adsorb cationic dyes MB or RhB

through electrostatic interactions. With the increase of the calcination temperature, the zeta potential value of the product became larger and larger, so the ability to adsorb MB gradually decreased. Among them, the zeta potential of TMO300 is the lowest ($\zeta = -53.1$ mV), so TMO300 has the best adsorption performance for MB.

To further study the adsorption mechanism of MB dyes on TMO300, the MB adsorbed on TMO300 was characterized by FTIR. In the FTIR spectrum of MB (Fig. 5), the peak at 1586 cm^{-1} corresponds to the vibration of the aromatic ring, the stretching vibration peaks of C–N are located at 1484 cm^{-1} and 1380 cm^{-1} , and the peak at 1311 cm^{-1} corresponds to the vibration of the CH_3 group.^{37,38} In addition, after TMO300 adsorbed MB, characteristic peaks related to MB appeared in the range of $1300\text{--}1600\text{ cm}^{-1}$, of which the peak at 1600 cm^{-1} corresponds to the vibration peak of the aromatic ring, and the peaks at 1487 cm^{-1} and 1384 cm^{-1} correspond to the stretching vibration of C–N, the peak at 1324 cm^{-1} correspond to the vibration peak of CH_3 group, indicating that TMO300 achieves effective adsorption of MB. After TMO300 adsorbed MB, the $\nu(W-O)$ peak of TMO300 moved from 586 cm^{-1} to 593 cm^{-1} , the $\nu(Mo-O)$ peak moved from 970 cm^{-1} to 1018 cm^{-1} , and the characteristic peaks related to MB also showed a degree shift, indicating that the adsorption of MB on TMO300 is due to the electrostatic interaction between MB and TMO300.³⁹

XPS was used to analyze element species and element valence before and after TMO300 adsorbed MB. For the full XPS spectrum of TMO300 with signal peaks related to W, Mo, C, and O, see supplementary Fig. S4a. For the full XPS spectrum of MB adsorption onto TMO300, see supplementary Fig. S4b, and a new N1s signal peak at 400 eV is found, indicating that TMO300 effectively adsorbs

MB. Before the adsorption of MB, the W4f and W5p of TMO300 can be fitted with three curves (see supplementary Fig. S4c), with peaks at 35.49 eV , 37.34 eV , and 41.03 eV , corresponding to W4f7/2, W4f5/2, and W5p3/2, respectively, indicating that W atoms exist in the form of +6 valence. The Mo3d high-resolution energy spectrum of TMO300 (see supplementary Fig. S4e) consists of two spin-orbit splitting peaks at 232.79 eV and 235.97 eV , corresponding to Mo3d5/2 and Mo3d3/2, respectively, indicating that Mo atoms exist in the form of +6 valence. The O1s characteristic peak at 530.7 eV is attributed to lattice oxygen (W–O–Mo), and the peak at 532.2 eV is related to adsorbed water (H_2O) (see supplementary Fig. S4g). After TMO300 adsorbed MB, the signal peaks of O1s, W4f, W5p, and Mo3d change to different degrees in the direction of low binding energy, indicating the existence of electrostatic interaction.

In general, the above synergistic effect of the above aspects makes TMO300 have a high adsorption capacity for cationic dyes.

Selective Adsorption Performances

The selective adsorption behavior of the best adsorbent TMO300 was explored. The preferential adsorption and separation of specific dyes in mixed dyes are more attractive to the adsorption properties. MB, RhB, and MO are selected to prove the adsorption priority of dyes because they have different molecular radii, surface charges, and functional groups.³⁹ TMO300 exhibits electronegativity ($\zeta = -53.1$ mV) in a neutral aqueous solution, while MB and RhB have positive charges on the surface. Due to electrostatic adsorption, it is judged that TMO300 has a good adsorption capacity for MB and RhB.

As displayed in Fig. 6a, within 120 min, the adsorption rate of TMO300 for MB was up to

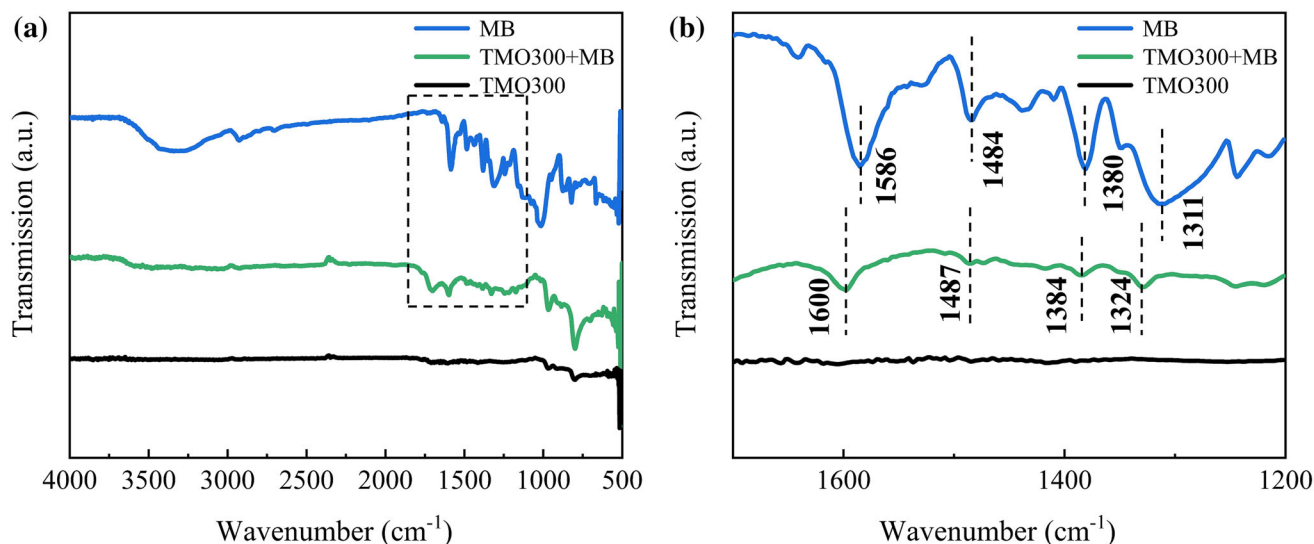


Fig. 5. (a) FTIR spectra of MB and TMO300 before and after adsorption of MB; (b) enlarged image of the zone marked in (a).

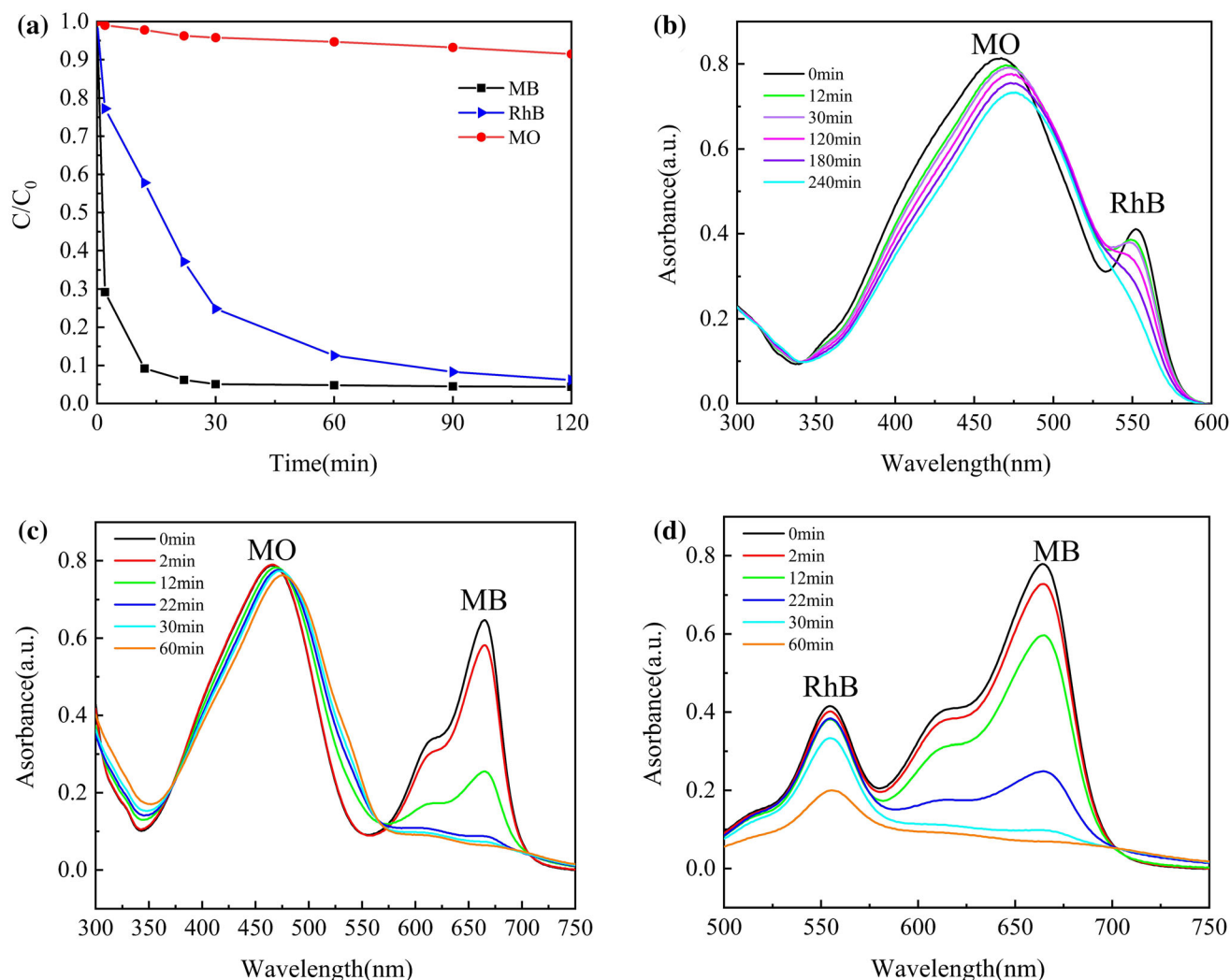


Fig. 6. The time-dependent curve of the adsorption efficiency of MB, MO, and RhB by TMO300 (a) and the UV-Vis absorption spectra of the mixture solution under different time intervals: (b) RhB and MO; (c) MB and MO; (d) MB and RhB.

95.6%, and the adsorption equilibrium could be reached in about 30 min. The adsorption rate of RhB was 93.5%, and the adsorption equilibrium was reached in about 120 min. The adsorption rate of MO was the worst; only 8.53% can be adsorbed. Compared with the anionic dye MO, TMO300 has a good adsorption capacity for cationic dyes such as MB and RhB. As for the adsorption equilibrium time, the adsorption capacity of TMO300 for MB is better than RhB.

Figure 6b, c, and d shows the selective adsorption properties of TMO300 for a mixed solution of two dyes. Figure 6b and c shows that the adsorption rate of TMO300 for MB and RhB is much higher than that for MO. In Fig. 6d, the adsorption rates of TMO300 for MB and RhB in 60 min are 91.4% and 84.4%, respectively. It is further shown that among the mixed dyes, TMO300 has the better adsorption property for cationic dyes. However, among mixed dyes, the adsorption rate of TMO300 to various dyes is generally lower than that in the single dye

solution; this is because the active sites in TMO300 are limited, and the active sites are shared by different dyes, resulting in a lower adsorption rate than that for a single dye. In the case of double cationic dyes, the adsorption rate of TMO300 for MB is higher than that for RhB. This is because the molecular size of RhB is larger than MB,⁴⁰ so there is a larger steric hindrance, which reduces the adsorption capacity of RhB.

Reusability of TMO300

A sustainable adsorption material not only has considerable selective adsorption and adsorption capacity but also shows good reusability. To investigate the reuse of TMO300 on MB, six adsorption-desorption cycles were carried out. After the adsorption of MB, TMO300-MB was calcined at 300°C for 30 min to decompose the adsorbed MB, while TMO300 was stable at this temperature. The FTIR test (Fig. 7a) showed that the characteristic peaks associated with MB disappeared after calcination,

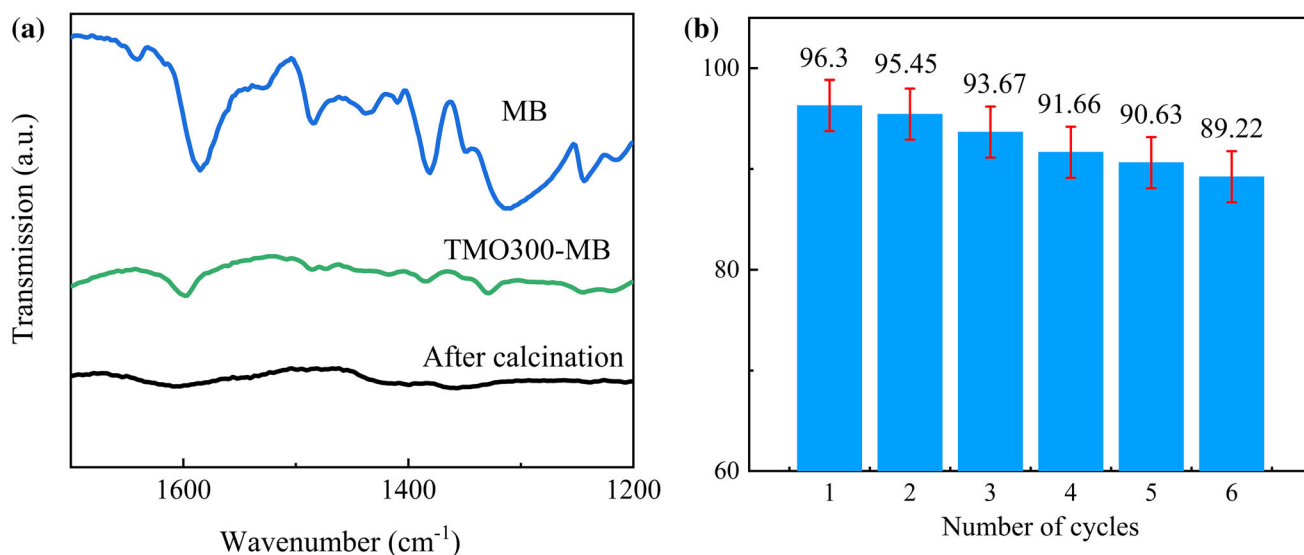


Fig. 7. (a) FTIR spectra of different samples. (b) Reusability of TMO300 for adsorption of MB.

implying the adsorbate has been decomposed. As shown in Fig. 7b, in the previous five cycles, the adsorption rate of TMO300 to MB was 96.3%, 96.3%, 95.45%, 93.67%, 91.66%, and 90.63%, respectively. In the last cycle experiment, the adsorption rate of TMO300 to MB can reach 89.22%. After each cycle experiment, the adsorption rate of TMO300 to MB decreased a little, which was due to the small loss of the adsorbent in the recovery process. The above results show that most of the adsorbed MB can be desorbed, and TMO300 has good cycling ability, which can be used as a potential renewable adsorbent to remove cationic water pollutants.

Adsorption Properties of Products with Different W/Mo Molar Ratios

Among all the products with a primary W/Mo molar ratio of 1:1, the one produced at 300°C (TMO300) shows better adsorption performance than those calcined at different temperatures. To investigate the adsorption performance of TMOs with different primary W/Mo molar ratios, products were calcined at 300°C with the primary W/Mo molar ratio of 0.5:1, 1.5:1, 1.75:1, and 2:1, respectively. The preparation method of tungsten molybdenum oxide was the same as the preparation method in “Synthesis” section. These products are named after the ratio, such as TMO0.5, TMO1.5, TMO1.175, and TMO2.

TMO0.5, TMO1.5, TMO1.175, and TMO2 of 10 mg were respectively added to 10 mg/L 100 mL MB solution to test the adsorption performance. Figure 8 shows the comparison of the adsorption performance for MB of TMO0.5, TMO1.5, TMO1.175, TMO2, and TMO300 (= TMO1). It can be seen that TMO300 has the highest adsorption rate for MB within 300 min, which is 96.83%, so it

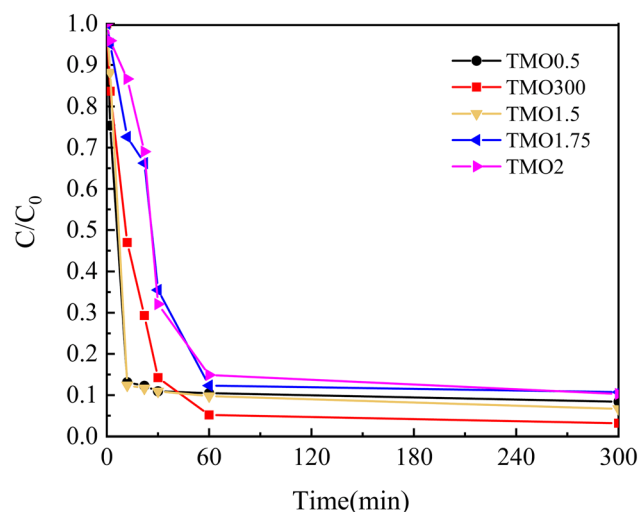


Fig. 8. Time-dependent curve of MB concentration in different samples.

can be inferred that the adsorption performance is optimal when the primary W/Mo molar ratio is 1:1.

Recovery of W-Mo Alloy Scrap

Recovery Process

The W-Mo alloy scrap was placed in a crucible with a certain amount of NaOH and calcined at 600°C for 2 h. After that, 40 mL of deionized water was added to the crucible, and the mixture was stirred in a 60°C water bath for 2 h to get the leaching solution. Then, insoluble impurities from the W-Mo alloy scrap in the leaching solution were removed by centrifugation, and the existing state of W and Mo in the solution was the same as that of the simulated leaching solution mentioned in “Synthesis” section. Then, the preparation method of

tungsten molybdenum oxide was the same as that for the simulated W and Mo ion solution. These tungsten molybdenum oxide products were named after the calcination temperature, such as TMO*300 and TMO*600.

Structure, Morphology, and Performance

Comparing Fig. 9a and b shows that the morphology of the W-Mo alloy scrap is both spherical and flake-like before recycling, but the flake diameter is < 500 nm. The morphology of TMO*300 is flaky and uneven, and there is a certain degree of agglomeration, which is very similar to TMO300.

The XRD pattern and elemental compositions of W-Mo alloy scraps can see supplementary Fig. S2 and Table S4. It can be seen that the proportion of W and Mo in the alloy scrap is relatively high. Figure 9c shows the XRD diagram of TMO*300 and TMO*600. It can be seen that TMO*300 has poor crystallinity and is an amorphous phase. There are strong peaks in TMO*600 spectra at 23.09° , 23.58° , 24.30° , 33.50° , and 34.53° , which are consistent with

the orthorhombic phase $W_{0.4}Mo_{0.6}O_3$ (JCPDS no. 76-1280), and their strong peaks corresponding to crystal planes are (110), (002), (111), (200), and (112), respectively. Among them, the corresponding peaks of (002) and (111) shift to the left because of the lattice distortion caused by the macroscopic residual stress in the sample.

TMO*300 of 10 mg was added to a 100 mL MB solution of 10 mg/L, and the adsorption performance was tested. The comparison of the adsorption performance to MB between TMO*300 and TMO300 is displayed in Fig. 9d. The adsorption equilibrium time of TMO*300 and TMO300 to MB is almost the same as 30 min. At 60 min, the adsorption rate of TMO*300 for MB was not much different from that of TMO300, which was 94%.

The structural, morphology, and performance characterization show that the method of recovering W-Mo alloy waste is feasible, and the prepared tungsten molybdenum oxide has good selective adsorption properties for cationic dyes and has great potential in environmental remediation.

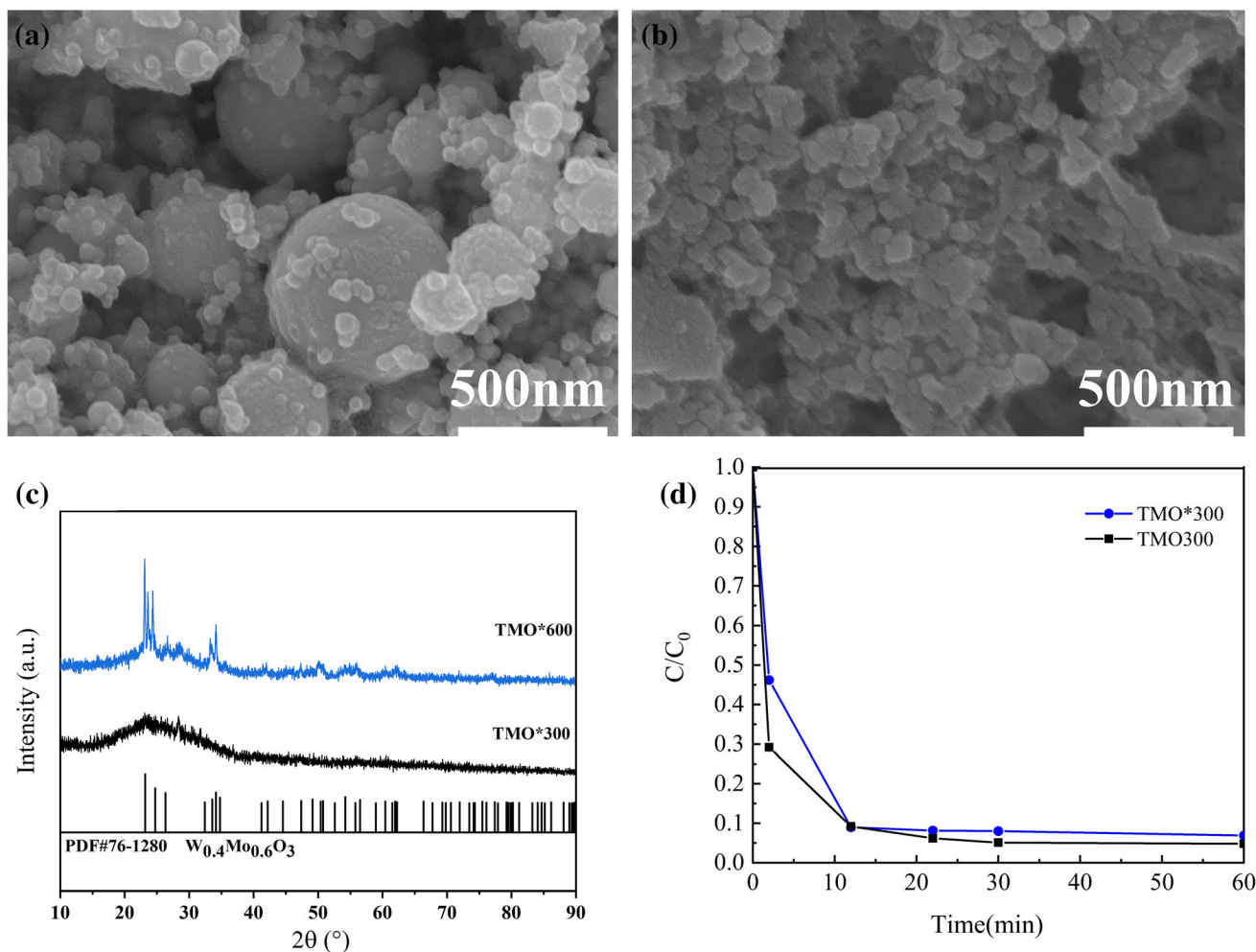


Fig. 9. (a) SEM image of W-Mo alloy scrap and (b) TMO*300; XRD diagram (c) and (d) adsorption properties of TMO*300 and TMO300.

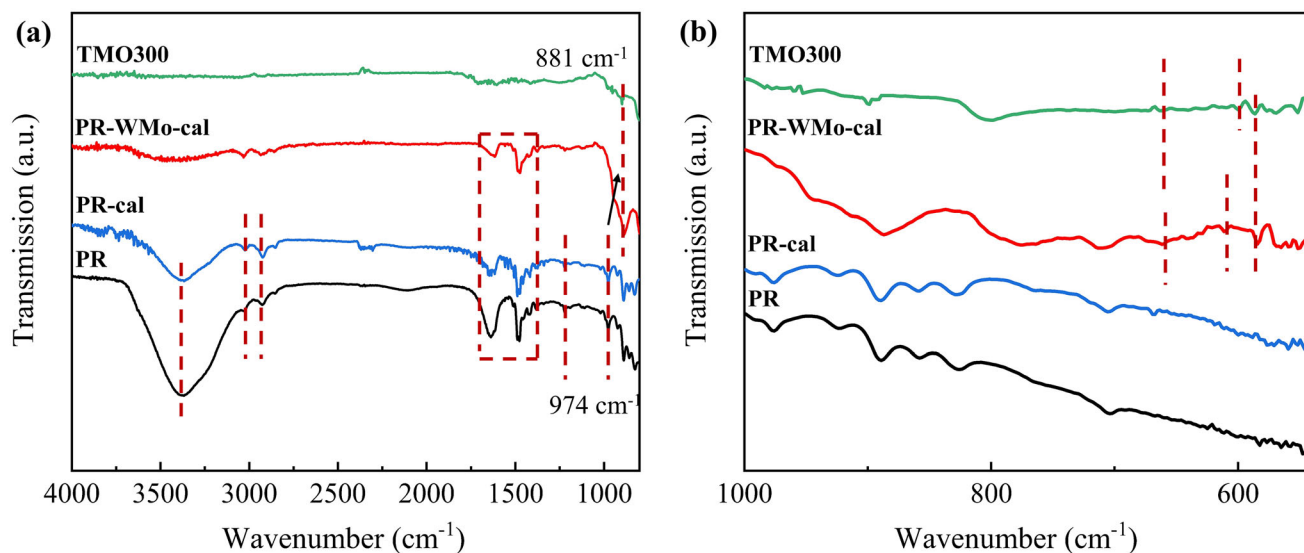


Fig. 10. (a) FTIR spectra of different samples; (b) FTIR spectra from 500 cm^{-1} to 1000 cm^{-1} of different samples.

Formation Mechanism of $W_{0.4}Mo_{0.6}O_3$

To explain the formation mechanism of the sample, different samples tested by FTIR are shown in Fig. 10. The pristine resin, the pristine resin that has been calcined once, and the pristine resin that has been calcined once after adsorption of molybdenum and tungsten ions are named PR, PR-cal, and PR-WMo-cal, respectively.

The FTIR spectra of the PR and PR-cal (Fig. 10a) show that the intensity of the peak of hydroxyl (3420 cm^{-1}), quaternary amino group (974 cm^{-1}), $-CH_2-$ (2942 cm^{-1}), $-CH_3-$ (3028 cm^{-1}), benzene ring (1640 cm^{-1} , 1484 cm^{-1}), and C-N (1219 cm^{-1}) decreases slightly after calcination, and the content of H and O reduces obviously. Comparing the PR-WMo-cal with the PR shows that the characteristic peak of CH_2- , $-CH_3-$, $-C-N-$, and benzene ring still exists, but the peak area is reduced, indicating that its content is reduced, which shows that the original components of the pristine resin cannot be removed totally by calcination for one time. Figure 10a also shows that the quaternary amine groups of PR-cal and PR appear at 974.1 cm^{-1} , but the quaternary amine groups of PR-WMo-cal and TMO300 appear at 881.7 cm^{-1} , producing a red shift. This red shift is attributed to the formation of tungsten-molybdenum heteropolyacids, in which the oxygen atom combines with more electronegative nitrogen atoms to obtain a higher electron density.

The peaks in the range of $500\text{--}1000\text{ cm}^{-1}$ correspond to the stretching and bending vibrations of the W-O and the Mo-O, as shown in Fig. 10b. PR-WMo-cal has characteristic peaks at 584 cm^{-1} and 660 cm^{-1} , which are the stretching vibration of W-O. A peak is also found at about 610 cm^{-1} , which is the stretching vibration peak of Mo-O. Therefore, it can be inferred that both W and Mo are successfully adsorbed on the resin and turned into $W_{0.4}Mo_{0.6}O_3$ through calcination.

CONCLUSION

The similar nature of W and Mo makes the separation and recovery of W and Mo scrap difficult. W and Mo ions in the leaching solution of W-Mo alloy scrap can be captured by ion-exchange resin without separation, and $W_{0.4}Mo_{0.6}O_3$ can be obtained by the simple heat-treatment process of the adsorbed resin. The calcination temperature has an important effect on the crystallinity and morphology of the products. The adsorption process of the sample calcined at 300°C with the W/Mo ratio of 1:1 (TMO300) to MB fits well with the Langmuir model and the pseudo-second-order model, which is surface-controlled monolayer adsorption. TMO300 shows superior selective adsorption capacity of MB, which can reach 833.43 mg/g in a neutral condition with excellent reusability, and the adsorption rate for MB can still be maintained at 89.22% in the sixth cycle experiment. $W_{0.4}Mo_{0.6}O_3$ with similar adsorption properties can be prepared from W-Mo alloy scrap by the same method.

This work not only provides a new and promising adsorbent for the adsorption and removal of wastewater but also realizes a short process method from metal waste to functional products, which not only opens up a new way for the recovery and reuse of secondary resources but also develop new material for removing organic pollutants.

SUPPLEMENTARY INFORMATION

The online version contains supplementary material available at <https://doi.org/10.1007/s11837-023-05929-w>.

ACKNOWLEDGEMENTS

This work was financially supported by Beijing Natural Science Foundation (no. 2202010), National Natural Science Foundation of China (no. 51702008), National Natural Science Foundation of China for Distinguished Young Scholar (no. 52025042), and National Natural Science Foundation of China for Innovative Research Groups (no. 51621003).

CONFLICT OF INTERESTS

On behalf of all authors, the corresponding author states that there is no conflict of interest.

REFERENCES

- E. Grigore, C. Ruset, M. Gherendi, D. Chioibas, and A. Hakola, *Phys. Scr.* T167, 014028 <https://doi.org/10.1088/0031-8949/t167/1/014028> (2016).
- J. Wang, M. Yi, C. Xu, G. Xiao, Z. Chen, J. Zhang, and L. Wang, *Int. J. Refract. Met. Hard Mater.* 99, 105607 <https://doi.org/10.1016/j.jrmhm.2021.105607> (2021).
- J.L. Clausen, and N. Korte, *Sci. Total Environ.* 407, 2887 <https://doi.org/10.1016/j.scitotenv.2009.01.029> (2009).
- Q.-C. Liu, M. Cui, Q.-K. He, Z.-Y. Liu, Y. Liang, K. Xie, and J.-Q. Sun, *Eng. Fail. Anal.* 89, 37 <https://doi.org/10.1016/j.engfailanal.2018.02.024> (2018).
- R.N. Chauhan, N. Tiwari, H.-P.D. Shieh, and P.-T. Liu, *Mater. Lett.* 214, 293 <https://doi.org/10.1016/j.matlet.2017.12.020> (2018).
- W. Sun, S. Zhou, Y. Sun, Y. Xu, and H. Zheng, *J. Environ. Chem. Eng.* 9, 104681 <https://doi.org/10.1016/j.jece.2020.10.4681> (2021).
- C. Michail, V. Koukou, N. Martini, G. Saatsakis, N. Kalyvas, A. Bakas, I. Kandarakis, G. Fountos, G. Panayiotakis, and I. Valais, *Crystals* 10, 429 <https://doi.org/10.3390/cryst10060429> (2020).
- S.P. Preval, N.R. Badnell, and M.G. O'Mullane, *Phys. Rev. A* 93, 042703 <https://doi.org/10.1103/PhysRevA.93.042703> (2016).
- S. Abbas, M.K.G. Shiran, K. Amini, H. Bakhtiari, and B. Samimi, *Prot. Met. Phys. Chem. Surf.* 55, 942 <https://doi.org/10.1134/s2070205119050228> (2019).
- X. Wang, G. Brunetti, W. Tian, G. Owens, Y. Qu, C. Jin, and E. Lombi, *Environ. Pollut.* 269, 116132 <https://doi.org/10.1016/j.envpol.2020.116132> (2021).
- M.U. Arshad, H. Raza, M.B. Khan, and A. Hussain, *Polym. Test.* 90, 106646 <https://doi.org/10.1016/j.polymertesting.2020.106646> (2020).
- M. Zhang, H. Song, C. Zheng, Z. Lin, Y. Liu, W. Wu, and X. Gao, *J. Air Waste Manag. Assoc.* 70, 971 <https://doi.org/10.1080/10962247.2020.1792377> (2020).
- J. Wang, S. Ren, Z. Li, C. Wang, X. Huang, C. Fu, L. Zheng, and T. Ren, *Tribol. Int.* 159, 106988 <https://doi.org/10.1016/j.triboint.2021.106988> (2021).
- T.B. Yaqub, K. Hebbur Kannur, T. Vuchkov, C. Pupier, C. Héau, and A. Cavaleiro, *Mater. Lett.* 275, 128035 <https://doi.org/10.1016/j.matlet.2020.128035> (2020).
- Z. Han, A. Golev, and M. Edraki, *Minerals* 11, 701 <https://doi.org/10.3390/min11070701> (2021).
- WBMS, *World Metal Statistics Yearbook* (WBMS, London, 2020).
- Z. Li, J. Lu, S. Wu, G. Zhang, W. Guan, L. Zeng, Q. Li, and Z. Cao, *ACS Sustain. Chem. Eng.* 8, 6914 <https://doi.org/10.1021/acssuschemeng.9b06383> (2020).
- F. Guo, X. Xi, L. Ma, and Z. Nie, *J. Clean. Prod.* 335, 130304 <https://doi.org/10.1016/j.jclepro.2021.130304> (2022).
- B. Ghadai, P.C. Rout, D. Mohapatra, B. Padh, and B.R. Reddy, *Hydrometallurgy* 191, 105237 <https://doi.org/10.1016/j.hydromet.2019.105237> (2020).
- Y. Zhang, Y. Lei, W. Ma, Z. Shi, Q. Chen, Z. Li, and C. Wang, *Chem. Eng. J.* 430, 132916 <https://doi.org/10.1016/j.cej.2021.132916> (2022).
- Q. Liang, H. Yue, W. Zhou, Q. Wei, Q. Ru, Y. Huang, H. Lou, F. Chen, and X. Hou, *Chemistry* 27, 14225 <https://doi.org/10.1002/chem.202102015> (2021).
- B. Deng, Z. Zhou, W. Wang, and D. Wang, *ACS Sustain. Chem. Eng.* 8, 14022 <https://doi.org/10.1021/acssuschemeng.0c03989> (2020).
- R. Swiderska-Dabrowska, K. Piaskowski, and P.K. Zarzycki, *J. AOAC Int.* 101, 1429 <https://doi.org/10.5740/jaoacint.18-0060> (2018).
- S. Zhang, H. Li, and Z. Yang, *J. Alloys Compd.* 722, 555 <https://doi.org/10.1016/j.jallcom.2017.06.095> (2017).
- S. Adhikari, S. Mandal, D. Sarkar, D.-H. Kim, and G. Madras, *Appl. Surf. Sci.* 420, 472 <https://doi.org/10.1016/j.apsusc.2017.05.191> (2017).
- S.A. Kuznetsova, O.S. Khalipova, K.V. Lisitsa, A.A. Ditts, A.G. Malchik, Y.W. Chen, and V.V. Kozik, *J. Appl. Polym. Sci.* 138, 50851 <https://doi.org/10.1002/app.50851> (2021).
- P. Mei, M. Yang, Y. Bai, S. Fei, Y. Dong, and H. Cheng, *J. Catal.* 360, 213 <https://doi.org/10.1016/j.jcat.2018.02.004> (2018).
- S. Yoon, and A. Manthiram, *J. Mater. Chem.* 21, 4082 <https://doi.org/10.1039/c0jm04571c> (2011).
- P. Jia, H. Tan, K. Liu, and W. Gao, *Int. J. Mod. Phys. B* 31, 1744099 <https://doi.org/10.1142/s0217979217440994> (2017).
- G.I. Supelano, J.A. Gómez Cuaspu, L.C. Moreno-Aldana, C. Ortiz, C.A. Trujillo, C.A. Palacio, C.A. Parra Vargas, and J.A. Mejía Gómez, *Fuel* 263, 116800 <https://doi.org/10.1016/j.fuel.2019.116800> (2020).
- L. Chen, and B. Bai, *Ind. Eng. Chem. Res.* 52, 15568 <https://doi.org/10.1021/ie4020364> (2013).
- K.Y. Foo, and B.H. Hameed, *Chem. Eng. J.* 156, 2 <https://doi.org/10.1016/j.cej.2009.09.013> (2010).
- N. Le Houx, *J. Phys. Chem. C* 114, 155 <https://doi.org/10.1021/jp908669u> (2010).
- X. Zhang, A. Li, Z. Jiang, and Q. Zhang, *J. Hazard. Mater.* 137, 1115 <https://doi.org/10.1016/j.jhazmat.2006.03.061> (2006).
- B. Liu, J. Wang, J. Wu, H. Li, Z. Li, M. Zhou, and T. Zuo, *J. Mater. Chem. A* 2, 1947 <https://doi.org/10.1039/c3ta13897f> (2014).
- Y. Li, X. Yin, X. Huang, J. Tian, W. Wu, and X. Liu, *Appl. Surf. Sci.* 495, 143626 <https://doi.org/10.1016/j.apsusc.2019.143626> (2019).
- H. Li, F. Xie, W. Li, B.D. Fahlman, M. Chen, and W. Li, *RSC Adv.* 6, 105222 <https://doi.org/10.1039/c6ra22414h> (2016).
- Z. Li, P.-H. Chang, W.-T. Jiang, J.-S. Jean, and H. Hong, *Chem. Eng. J.* 168, 1193 <https://doi.org/10.1016/j.cej.2011.02.009> (2011).
- S. Khanam, and S.K. Rout, *Bull. Mater. Sci.* 44, 1 <https://doi.org/10.1007/s12034-020-02292-3> (2021).
- N. Mohammed, H. Lian, M.S. Islam, M. Strong, Z. Shi, R.M. Berry, H.-Y. Yu, and K.C. Tam, *Chem. Eng. J.* 417, 329 <https://doi.org/10.1016/j.cej.2021.129237> (2021).

Publisher's Note Springer Nature remains neutral with regard to jurisdictional claims in published maps and institutional affiliations.

Springer Nature or its licensor (e.g. a society or other partner) holds exclusive rights to this article under a publishing agreement with the author(s) or other rightsholder(s); author self-archiving of the accepted manuscript version of this article is solely governed by the terms of such publishing agreement and applicable law.